A three-dimensional thermal and fluid dynamics analysis of a gas cooled subcritical fast reactor driven by a D–T fusion neutron source

G. Angelo [a,b,*], D.A. Andrade [a], E. Angelo [a,b], T. Carluccio [a], P.C.R. Rossi [a], A. Talamo [c]

[a] Instituto de Pesquisas Energeticas e Nucleares, Avenida Lineu Prestes, 2242, Centro de Engenharia Nuclear, CEP 05508-000, São Paulo, SP, Brazil
[b] Instituto Presbiteriano Mackenzie, Rua da Consolação, 930, CEP 01302-907, São Paulo, SP, Brazil
[c] Argonne National Laboratory, Department of Nuclear Engineering, 9700 S. Cass Avenue, Argonne, IL 60439, United States

ABSTRACT

The entire nuclear fuel cycle involves partitioning classification and transmutation recycling. The usage of a tokamak as neutron sources to burn spend fuel in a gas cooled subcritical fast reactor (GCSFR) reduces the amount of long-lived radionuclide, thus increasing the repository capacity.

This paper presents numerical thermal and fluid dynamics analysis for a gas cooled subcritical fast reactor. The analysis aim to determine the operational flow condition for this reactor, and to compare three distinct turbulence models (Eddy Viscosity Transport Equation, standard k–ε and SSG Reynolds stress) for this application.

The model results are presented and discussed. The methodology used in this paper was developed to predict the coolant mass flow rate. It can be applied to any other gas cooled reactor.

© 2011 Elsevier Ltd. All rights reserved.

1. Introduction

Most of the sustainable industrial processes require their wastes to be classified and recycled. The entire nuclear fuel cycle involves partitioning classification and transmutation recycling (P&T). The main objective of P&T is to eliminate or at least to reduce the amount of such long-lived radionuclide, thus increasing the repository capacity (von Lensa et al., 2008).

The investigation of methods to P&T of long-lived radionuclide in spent nuclear fuel is strongly focused on accelerator driven hybrid systems (ADS) aiming the incineration of the spent nuclear fuel (Beller et al., 2001; Rubbia et al., 2001). Recently, the interest on fast reactors to burn up has increased and the concept of P&T has been incorporated into new reactor projects, generation IV (Abram and Ion, 2008) and INPRO (Omoto, 2005).

The possibility of utilization of tokamak as a neutron source for transmutation was investigated in a few papers (Parish and Davidson, 1980; Peng and Cheng, 1993; Gohar, 2001). The requirements for transmutation using a tokamak are lower than those for a pure fusion reactor (for electricity) due to neutron multiplication of the fission core (Parish and Davidson, 1980).

The utilization of three-dimensional computational fluid dynamics (CFD) codes has grown due to improvements in computer performance, to a greater range of available CFD softwares, and to the implementation of more robust solvers. The application of three-dimensional CFD in nuclear reactors has obstacles such as: (i) Complex geometries: the internal dimensions of a reactor can easily reach three orders of magnitude promoting an excessive number of elements. (ii) Turbulence models: although there is a wide range of turbulence models, they are not fully developed and they have distinct applications. (iii) Stratification: in some circumstances stratification processes may occur. (iv) Two-phase flow: there are several difficulties inherent to the two-phase flow (Ghorai and Nigam, 2006) as, for example, their complex behavior, due to the complex physics laws, their mathematical treatment and the fact that they require additional elaborated compatibility equations (closure problems). (v) Accident cases: (sudden transients) that completely differ from the operating conditions can also occur.

This paper presents numerical thermal and fluid dynamics analysis for the gas cooled subcritical fast reactor studied by Carluccio et al. (2011). The analysis aim to determine the operational flow condition for the GCSFR, and to compare three distinct turbulence models (Eddy Viscosity Transport Equation, standard k–ε and SSG Reynolds Stress) for this application. ANSYS-CFX code is used as the CFD tool.

2. Gas cooled subcritical fast reactor concepts

The GCSFR contains 384 fuel pins in a hexagonal arrangement, and a total of 245 fuel elements surrounding the tokamak. Fig. 1

---

* Corresponding author at: Instituto de Pesquisas Energeticas e Nucleares, Avenida Lineu Prestes, 2242, Centro de Engenharia Nuclear, CEP 05508-000, São Paulo, SP, Brazil. Tel.: +55 11 20848478; fax: +55 11 29187361.
E-mail addresses: gabriel.angelo@usp.br (G. Angelo), delvonei@ipen.br (D.A. Andrade), eangelo@mackenzie.br (E. Angelo), carluccio@usp.br (T. Carluccio), pcrrossi@ipen.br (P.C.R. Rossi), alby@anl.gov (A. Talamo).
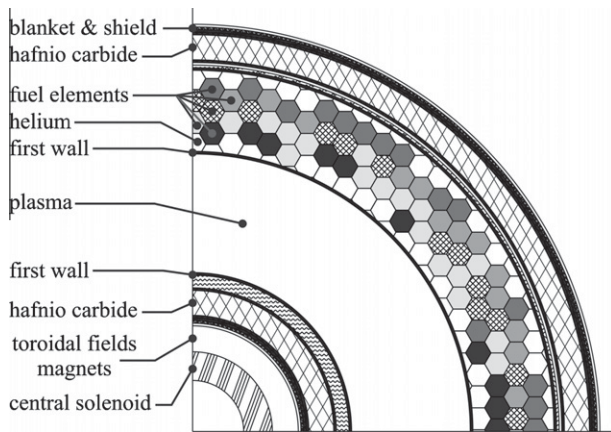
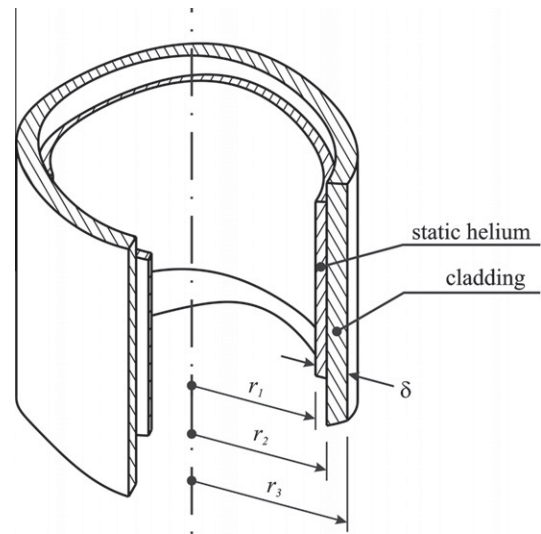**Fig. 1.** Cross section view of one quarter of the fusion driven GCSFR.

shows a cross section view of one quarter of the fusion driven GCSFR.

Each fuel particle is composed by a coated transuranic oxide kernel (TRU) surrounded by a silicon carbide (SiC) porous buffer intermediate zone and a SiC shell. The fuel particles are dispersed in a SiC matrix which is enclosed by an inert gas (helium gap) and a cladding structure composing the fuel pin, this design is based in a standard pressurized water reactor. The cladding material is HT-9 steel.

The reactor periodic pins assembly is shown in Fig. 2a. Fig. 2b illustrates a cross section detail view of the coolant channel. The location (1) is its center. Fig. 2c shows a cross section and the main dimensions of a single periodic fuel pin. The total length of the channel is 3 m. The geometry shown in Fig. 2c can also be divided into six equal symmetric parts as shown in Fig. 2d.

The melting point of the coated transuranic oxide kernel, the silicon carbide matrix and the HT-9 are 2000 °C (Stacey et al., 2005), 2700 °C (Patnaik and Knovel, 2003) and 1475 °C (Foulds, 1986), respectively. However, the maximum design temperature for nuclear reactors that use HT-9 as cladding material is about 565 °C (Klueh, 2009) due to creep strength.

3. Methodology

A tridimensional model was developed based on Fig. 2d, using the finite volume method applied to a hexahedral structured mesh (Maliska, 1994; Anderson and Wendt, 1995).

Fig. 3. Static helium and cladding isometric draw with geometrical description.

The equations considered are the mass, momentum and energy conservation. To ensure the consistency of the results, three different turbulence models were selected as follows: Eddy Viscosity Transport Equation (EVTE) (Durbin et al., 2001), standard k–ε (Launder and Spalding, 1974) and SSG Reynolds stress (Speziale et al., 1991).

The analysis considers helium as an ideal gas and the system at the steady state regime. Thus, density (ρ) is calculated by the ideal gas law as a function of temperature, according to Eqs. (1)–(3).

$$\rho = \frac{w \cdot p_{ABS}}{R_0 \cdot T}, \tag{1}$$

$$dh = c_p \cdot dT, \tag{2}$$

$$c_p = c_p(T), \tag{3}$$

where w is the molecular weight, p_{ABS} the absolute pressure, R_0 the universal gas constant, the enthalpy, c_p the specific heat capacity at constant pressure, and T the temperature.

The buoyancy effects and the conductive heat transfer in static helium were neglected.

The relationship between the helium layer plus the cladding (δ) and the total length of the channel (L) is approximately ($\delta/L = 2.5 \times 10^{-4}$). The explicit conceptions of these regions produce a significant increase in the elements number.
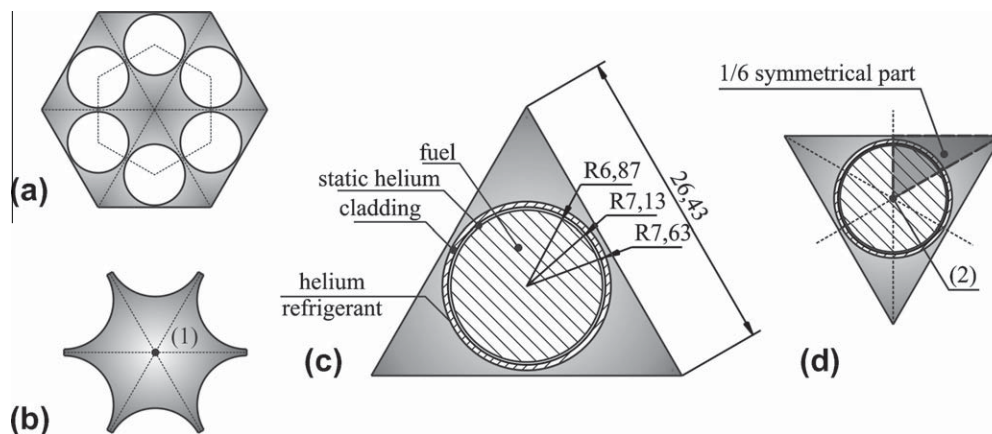

Fig. 2. (a) Sketch of the fuel pins in a periodic assembly, (b) cross section detailed view of the refrigerant channel, (c) cross section fuel pin, a portion of fluid and the main dimensions (all dimensions in millimeter), (d) indication of the six symmetric parts.
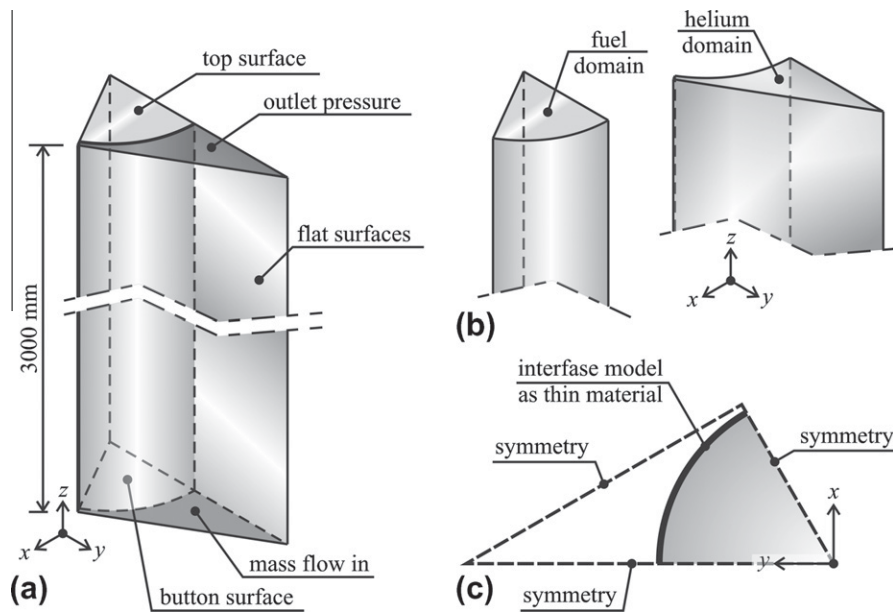
Fig. 4. (a) Three-dimensional schematic model of the computational domain, (b) detailed view of the fluid and solid domains ungrouped, and (c) two-dimensional detail showing the boundary conditions.

Methods for connecting different domains are costly in terms of computational time. In this case, at least three connection interfaces are required for the entire model. In order to avoid excessive computational time during the convergence process, the geometry between the fuel and the refrigerant (δ) was replaced. The thin surface technique was used to compute the heat transfer between fuel and coolant without explicitly creating sub-domains and additional contact interfaces.

The properties for the thin material were homogenized and the equivalent thermal conductivity was determined by Eq. (4). Thus the radius of the solid domain is the average between r_1 and r_3.

$$k_{eq} = \frac{\ln(r_3/r_1)}{\frac{\ln(r_2/r_1)}{k_{helium}} + \frac{\ln(r_3/r_2)}{k_{cladding}}} \qquad (4)$$

where r_1, r_2 and r_3 are shown in Fig. 3.

3.1. Boundary conditions

The computational domain and the regions descriptions are shown in Fig. 4. The fuel and the coolant domain can be observed separately in Fig. 4b. Fig. 4c shows a schematic cross section containing the boundary conditions.

The summary of the fluid domains boundary conditions is indicated in Table 1, and additional information is supported by Figs. 4a and c. The mass flow rate at the inlet location ($\dot{m}$) ranges from 0.003 kg/s to 0.01 kg/s. The static outlet pressure (p_{out}) was set

Table 1
Boundary conditions for coolant domain.

Location	Boundary condition
Button	Inlet mass flow rate 0.003 kg/s < $\dot{m}$ < 0.01 kg/s and inlet Helium temperature equals to 400 °C
Top	Outlet pressure set equal to 0 Pa (relative scale)
Curved surface	Conservative energy flux and wall no slip wall
Lateral flat surfaces	Symmetry
Reference pressure	7 MPa

Table 2
Boundary conditions for solid domain.

Location	Boundary condition
Top and button	Adiabatic Wall
Solid domain	Volumetric source term q''' for a hot channel (Fig. 4)
Curved surface	Conservative energy flux
Lateral flat surfaces	Symmetry

Table 3
Thermodynamics properties for solid domain.

Material	Property
Fuel	w_{FUEL} = 40.096 g/mol
	ρ_{FUEL} = 1.565 g/cm
	$c_{p\ FUEL}$ = 1.25 J/g K
	k_{FUEL} = 47.8 W/m K
Thin material	k_{EQ} = 0.723 W/m K

equal to 0 Pa (relative scale). Based on the hypothesis of using a direct Brayton cycle which utilizes the helium directly, the reference pressure was taken as 7 MPa (Stacey et al., 2005, 2006).

The boundary conditions for the solid domain are presented in Table 2. The thermodynamic properties for the fuel and the thin layer are constant and are given in Table 3.

The source term distribution is based on the neutron flux analysis by Carluccio et al. (2011) and is shown in Fig. 5. In this paper this same reactor is modeled with details in MCB, a continuous energy Monte Carlo code. MCB code is a patch of Monte Carlo N-Particle (MCNP) that allows burnup calculations. The neutron source was explicitly modeled in the MCB code. The fusion source is assumed isotropic and homogenous at the plasma region, with the typical D–T spectrum.

The average volumetric source term (q''') is equal to 43.3 MW/m³. Fig. 6 shows a contour map indicating the neutron flux per source neutron. One may clearly see that this will result in a different power distribution per pins. The peak factor was obtained by dividing the average value of this variable (on the entire domain) by its respective maximum value resulting in a peak factor equals to 1.959.
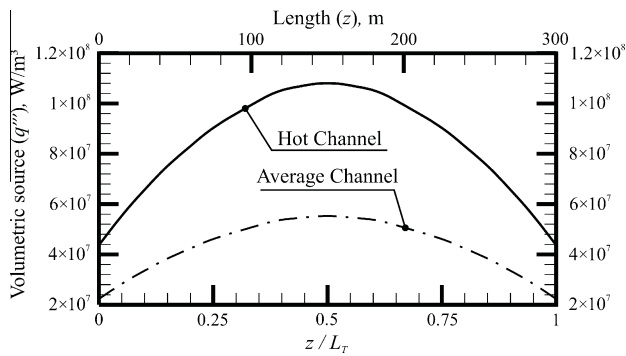
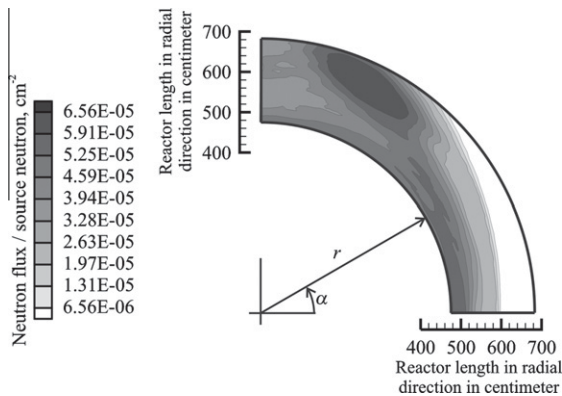**Fig. 5.** Axial volumetric source term as function of length.

Fig. 6. Neutron flux per source neutron, contour map.

3.2. Mesh

The numerical domain is composed of hexahedral and prismatic elements in a structured arrangement. The mesh was built using the Ansys ICEM CFD software.

Stern et al. (2001) and Wilson et al. (2001) present an approach to define and to verify the mesh, which is used in this paper. They discuss the mesh dependency on the results focusing the element size definition in order to validate the CFD models. The methodology considers an increase of the mesh density for the same boundary condition using predefined ratios. This procedure must be performed in such a way that property variation or small variations are not present. When this condition is satisfied the solution is considered independent of the mesh.

Fig. 7c shows a cross section of the mesh in the last interaction loop. A total of five meshes were created until the condition was satisfied. Fig. 7 shows two intermediate steps and the final mesh refinement.

Three independent variables were observed during the interactive processes: the average outlet temperature, the average outlet Mach number and the wall heat flux. These variables are shown in Fig. 8. Note that they have a clear tendency to constant values. The maximum variation found between the first and the last steps for any of these variables is less than 2%, thus indicating the results are independent of the mesh.

4. Results

In order to verify the consistency of the analysis three different turbulence models were tested. The comparison among the selected turbulence models is shown in Fig. 9. The central velocity and the central temperature z direction profiles are observed. A mass flow rate equals to 0.005 kg/s (with the average inlet velocity of 40 m/s approximately) and the volumetric energy source term equals to 43.3 MW/m^3 (for the average channel) were set as the boundary conditions for this analysis. The central temperature profiles have the same characteristics, magnitudes and behavior so that, any of the tested turbulence models may represent its characteristics. However, the central velocity profiles show a slight disagreement in $0.4 < z < 0.9$ m due to differences in the conceptions of the turbulence models.

All the turbulence models considered lead to consistent results, however, the SSG Reynolds stress model was chosen since it promotes a higher temperature gradient giving support to a conservative assumption.

The Eddy Viscosity based models consider analogy between the Reynolds stresses and viscous stresses (Eq. (5)). Turbulent heat flux
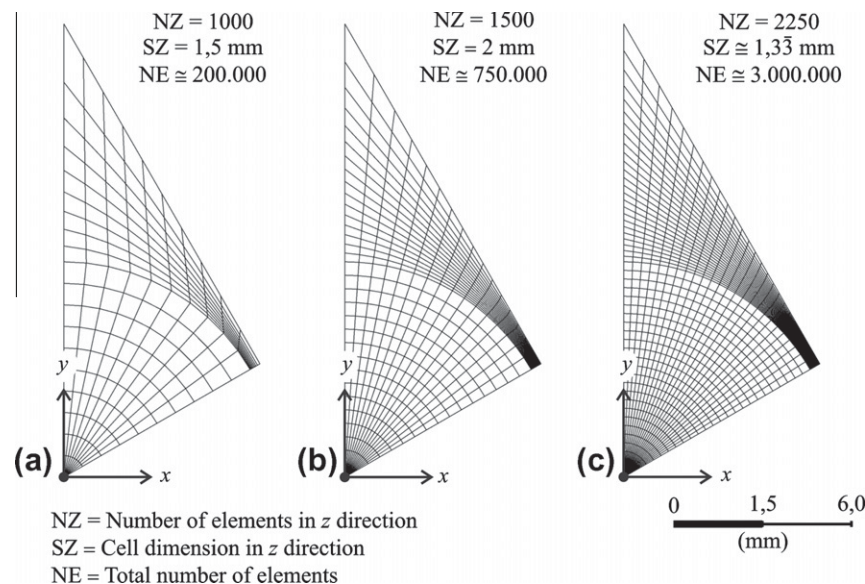

NZ = Number of elements in z direction
SZ = Cell dimension in z direction
NE = Total number of elements

Fig. 7. (a) Cross section of the computational domain for the first mesh, (b) cross section of the computational domain for the third mesh and (c) cross section of the computational domain for the fifth mesh.
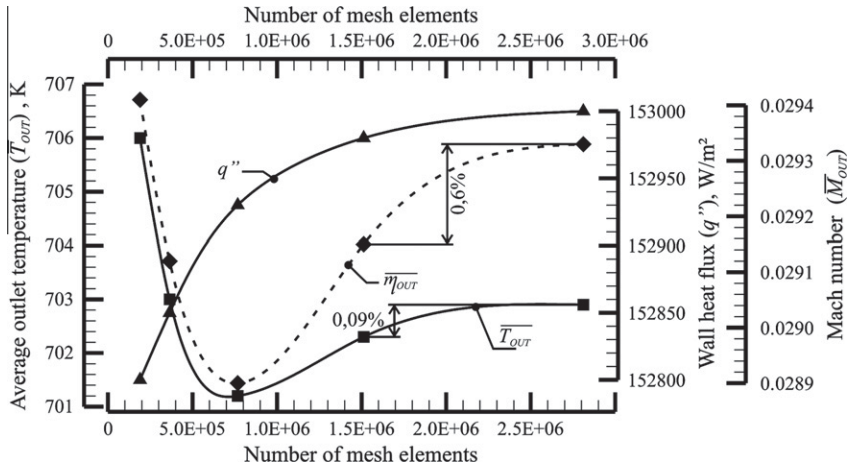
Fig. 8. Results as a function of the mesh elements number for an average channel.
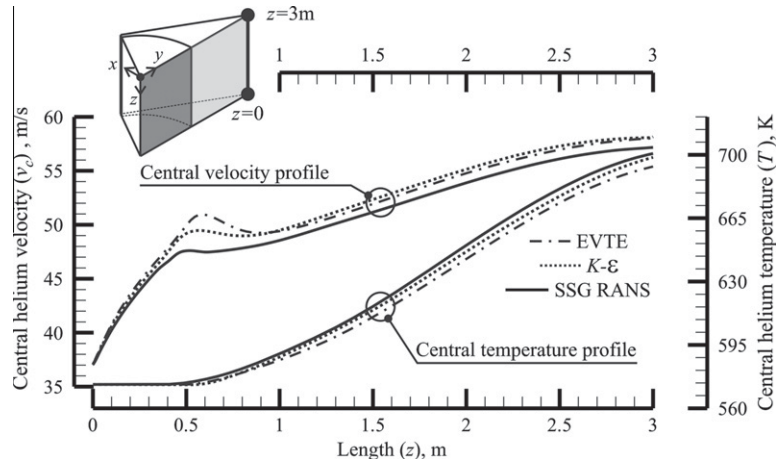

Fig. 9. Central coolant velocity profile and temperature profile as function of length for EVTE, KE and SSG Reynolds Stress turbulence models for an average channel.

for these models is obtained by mirroring the eddy-viscosity (Eq. (6)). On the other hand, a separate transport equation is solved for each of the six Reynolds stresses components in the SSG Reynolds Stress model.

$$\overline{u_i'u_j'} = -v_t\left(\frac{\partial \overline{U}_i}{\partial x_j} + \frac{\partial \overline{U}_j}{\partial x_i}\right) + \frac{2}{3}k\delta_{ij} + \frac{2}{3}v_t\frac{\partial \overline{U}_k}{\partial x_k} \tag{5}$$

where $\overline{U}$ is the average velocity, u' is the fluctuating velocity, v_t is the turbulent kinematic viscosity and k is the turbulent kinetic energy.

$$\overline{u_i'\theta'} = -\Gamma_t\frac{\partial \theta}{\partial x_i} \tag{6}$$

where is the θ temperature and Γ_t is the eddy diffusivity (Eq. (7)).

$$\Gamma_t = v_t\text{Pr}_t \tag{7}$$

where Pr_t is the turbulent Prandtl number.

The differences found in the central velocity profile and central temperature profile (Fig. 9) are justified by the behavior of the Reynolds stresses (Eqs. (8) and (9)). Fig. 10 shows the variable $\overline{(v'w')}_A$ and variable $\overline{(v'\theta')}_A$ as a function of channel length. Neglecting the lower order stresses $(\overline{u'v'}, \overline{u'w'})$ and lower order turbulent heat fluxes $(\overline{u'\theta'}, \overline{w'\theta'})$. The same range of the discrepancies presented

in Fig. 9 is verified in Reynolds stresses, so that, explaining this slight disagreement in 0.4 m < z < 0.9 m.

$$\overline{(u_i'u_j')}_A = \frac{1}{A}\int_A \overline{u_i'u_j'}dA \tag{8}$$

$$\overline{(u_i'\theta')}_A = \frac{1}{A}\int_A \overline{u_i'\theta'}dA \tag{9}$$

Fig. 11 shows the projection of the tangential velocity on the section where z/z_{max} = 0.2 (0.6 meters from origin) in order to visualize the
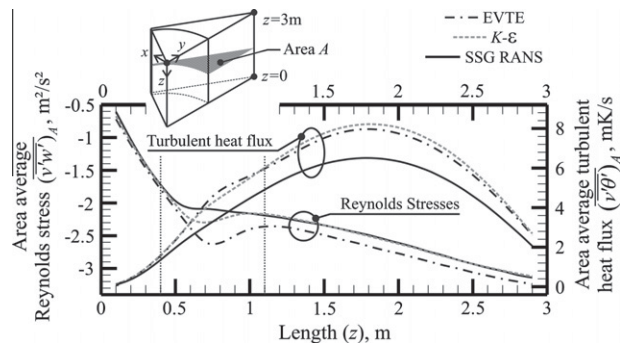

Fig. 10. Area average of main Reynolds stress $\overline{(v'\theta')}_A$ and area average of main the turbulent heat flux $\overline{(v'\theta')}_A$ as a function of length.
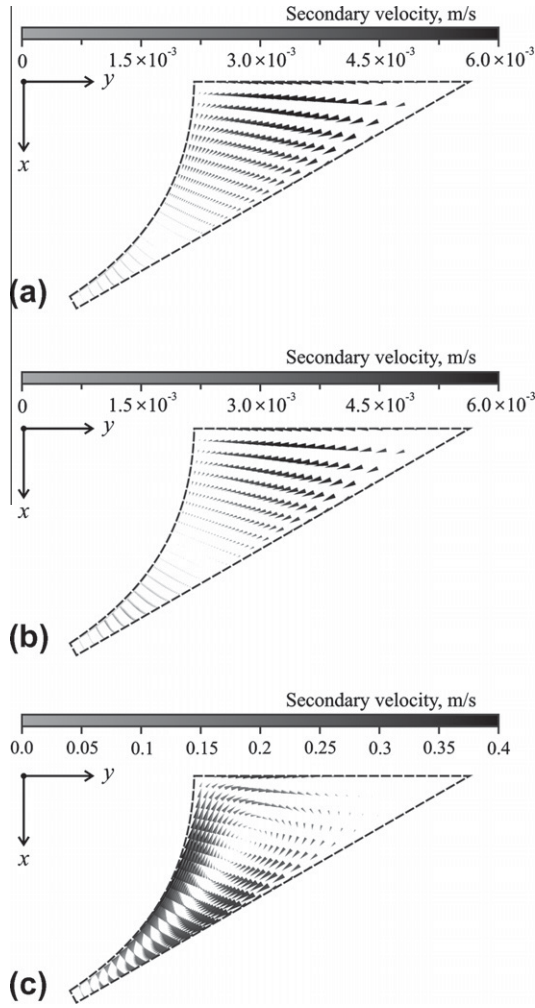
Fig. 11. Vector field comparison for the secondary flow on z/z_{max} = 0.2 section for an average channel, (a) EVTE, (b) standard k–ε and (c) SSG Reynolds Stress.

Fig. 12. Determination of the operational condition.

secondary flow for each turbulence model. While the relationship between the main and the secondary flow for the EVTE (Fig. 11a) and for the k–ε (Fig. 11b) are about 0.02% of the main flow, this relationship corresponds to approximately 1.3% for the SSG Reynolds Stress model (Fig. 11c). The EVTE and the k–ε models are not able to capture such effect, since there is no geometric abrupt variations in main flow direction (z).

In order to determine the limit of the mass flow rate for operational conditions four parameterizations were set, namely: the dimensionless fuel melting point (θ_{MF}), the dimensionless cladding melting point (θ_{MC}), the dimensionless cladding creep resistance (θ_C) and the dimensionless fluid temperature (θ_{He}), Eqs. (10)–(13).

$$\theta_{MF} = \frac{T_F^*}{T_{MF}}, \tag{10}$$

where T_F^* is the maximum fuel temperature (from numerical result) and T_{MF} is the fuel melting point.

$$\theta_{MC} = \frac{T_C^*}{T_{MC}}, \tag{11}$$

where T_C^* is the maximum cladding temperature (from numerical result) and T_{MC} is the cladding melting point.

$$\theta_C = \frac{T_C^*}{T_{CC}}, \tag{12}$$

where T_{CC} is the maximum temperature for creep strength (at 7 MPa).

$$\theta_{He} = \frac{(\overline{T_{out}} - T_{in})}{T_{in}} = \frac{\Delta T}{T_{in}}, \tag{13}$$

where T_{in} is the inlet temperature (boundary condition equals to 400 °C) and $\overline{T_{out}}$ is the area average outlet temperature.

Fig. 12 presents comparison for the results of each parameter as a function of the Reynolds number (Eq. (14)). The only threshold condition for a Reynolds number greater than 5.0×10^4 is the creep strength and this value should be at least 1.8×10^5, resulting in a mass flow rate of 0.053 kg/s per channel. The methodology used in this paper to predict the mass flow rate of the coolant can be applied to any other gas cooled reactor.

$$Re = \frac{\bar{\rho} \cdot V \cdot D_H}{\bar{\mu}}, \tag{14}$$

where the density ($\bar{\rho}$) and the dynamic viscosity ($\bar{\mu}$) are taken as the following averages over the entire fluid domain: $\bar{\rho} = \frac{\sum_{i=1}^{n} \rho_i \forall_i}{\forall}$ and $\bar{\mu} = \frac{\sum_{i=1}^{n} \mu_i \forall_i}{\forall}$.

The relationship between the Reynolds number and the Eckert number (Eq. 15) is indicated in Fig. 13. Note that a mass flow rate increment decreases the temperature gradient, leading to a descending behavior pattern. Fig. 13 also points out the Reynolds number as a function of Euler number (Eq. (16)). Since the Euler number indicates the relationship between kinetic and pressure energy the expected plot behavior is an ascending parabolic curve.

$$Ec = \frac{\overline{V}^2}{c_p \cdot (T_{out} - T_{in})}, \tag{15}$$

where $\overline{V}$ is the average inlet velocity.

$$Eu = \frac{\Delta p}{1/2 \cdot \bar{\rho} \cdot \overline{V}^2}, \tag{16}$$

where $\Delta p = (p_{in} - p_{out})$ and p_{in} and p_{out} are the average inlet and outlet pressure, respectively.

Fig. 14 presents Reynolds number, Eckert number and Euler number as function of the dimensionless coolant temperature (θ_{He}). An exponential behavior is verified by the curves $\theta_{He} = f(Re)$
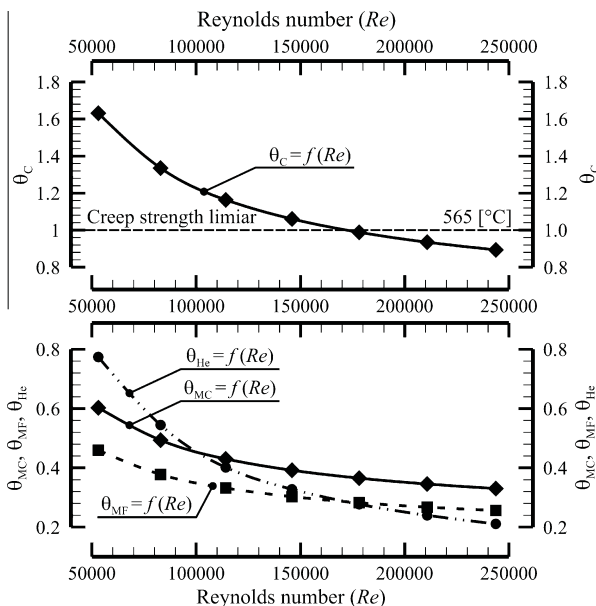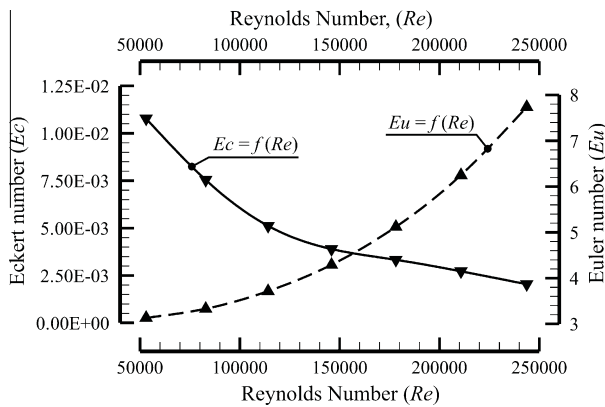
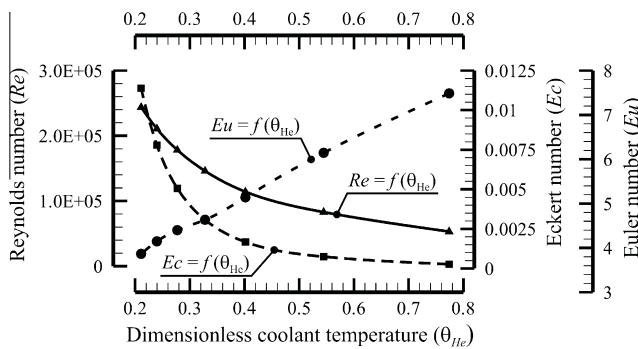**Fig. 13.** Euler and Eckert number as a function of Reynolds number.

Fig. 14. Reynolds number, Eckert number and Euler number as function of the dimensionless coolant temperature °C.
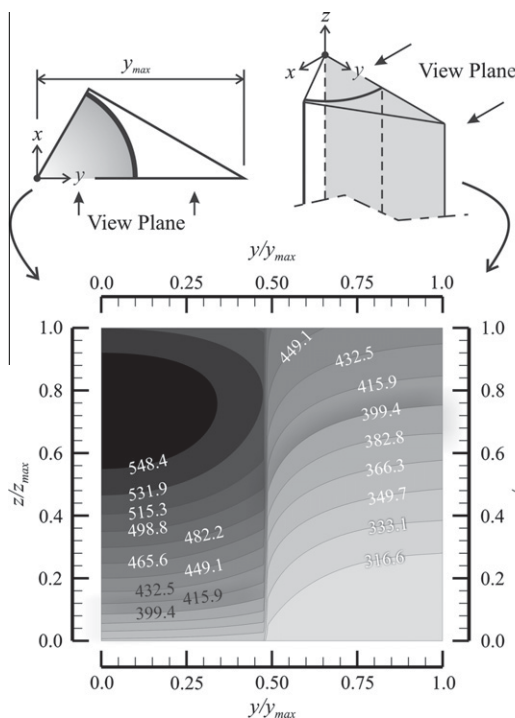

Fig. 15. Temperature contour plot for a fuel element (temperature in °C).

and $\theta_{He} = f(Ec)$, i.e., by increasing the kinetic energy of the coolant, the outlet temperature is exponentially reduced. A linear characteristic for the $\theta_{He} = f(Eu)$ is verified. This is due to the fact that

the Euler number can be indirectly interpreted as a friction factor. So, this linear correlation indicates an increase of the friction factor with viscosity by raising the system temperature.

Fig. 15 shows a temperature contour plot for 0.053 kg/s per channel as the operating condition. The temperature distribution and its development in the fluid channel can be observed.

5. Conclusions

A gas cooled subcritical fast reactor numerical model was successfully created through which the operational flow condition was determined.

A mesh composed of approximately three million of hexahedral and prismatic elements in a structure arrangement was created for the model.

The turbulence models: Eddy Viscosity Transport Equation, standard k–ε and SSG Reynolds Stress were investigated. The central velocity profiles in the range of 0.4 m < z < 0.9 m has shown small differences due to the conceptions of the turbulence models.

All turbulence models led to consistent results, however the SSG Reynolds Stress model was chosen as a conservative assumption, since it implied in slight higher temperature. Besides, it is capable to capture secondary flow effects.

The simulation was performed on a parallelized Intel® Xeon X3360 server which has a total of 8 cores. The total computational time for each steady state case was approximately: 2.9 h for the EVTE model, 4.8 h for the k–ε model and 6.8 h for the SSG Reynolds stress model.

Taking all cares in the creation of the model, passing through the mesh quality and mesh dependency this simulation led to consistent results since the dimensionless groups, Reynolds number, Euler number and Eckert number showed a good agreement with the classical physics literature.

The methodology, used in this paper, developed to predict the mass flow rate of the coolant, can be applied to any other gas cooled reactor.

References

Abram, T., Ion, S., 2008. Generation-IV nuclear power: a review of the state of the science. Energy Policy 36 (12), 4323–4330.

Anderson, J., Wendt, J., 1995. Computational Fluid Dynamics, vol. 206. McGraw-Hill.

Beller, D., Van Tuyle, G., Bennett, D., Lawrence, G., Thomas, K., Pasamehmetoglu, K., Li, N., Hill, D., Laidler, J., Fink, P., 2001. The US accelerator transmutation of waste program. Nuclear Instruments and Methods in Physics Research Section A: Accelerators, Spectrometers, Detectors and Associated Equipment 463 (3), 468–486.

Carluccio, T., Rossi, P., Angelo, G., Maiorino, J.R., Talamo, A., Gohar, Y., 2011. Comparison between two gas-cooled TRU burner subcritical reactors: fusion–fission and ADS. International Conference on Mathematics and Computational Methods Applied to Nuclear Science and Engineering Rio de Janeiro, 8 May.

Durbin, P., Reif, B., 2001. Statistical Theory and Modeling for Turbulent Flows. Wiley Online Library.

Foulds, J., 1986. Thermal history of HT-9 weldment heat-affected zones during welding. Journal of Nuclear Materials 141, 434–438.

Ghorai, S., Nigam, K., 2006. CFD modeling of flow profiles and interfacial phenomena in two-phase flow in pipes. Chemical Engineering and Processing 45 (1), 55–65.

Gohar, Y., 2001. Fusion solution to dispose of spent nuclear fuel, transuranic elements, and highly enriched uranium. Fusion Engineering and Design 58, 1097–1101.

Klueh, R., 2009. Ferritic/martensitic steels for advanced nuclear reactors. Transactions of the Indian Institute of Metals 62 (2), 81–87.

Launder, B., Spalding, D., 1974. The numerical computation of turbulent flows. Computer Methods in Applied Mechanics and Engineering 3 (2), 269–289.

Maliska, C., 1994. Transferência de calor e mecânica dos fluidos computacional: fundamentos e coordenadas generalizadas. Livros Técnicos e Científicos.

Omoto, A., 2005. Nuclear power for sustainable development and relevant IAEA activities for the future. Progress in Nuclear Energy 47 (1-4), 16–26.

Parish, T., Davidson, J., 1980. Reduction in the toxicity of fission product wastes through transmutation with deuterium–tritium fusion neutrons. Nuclear Technology (United States) 47 (2).

Patnaik, P., Knovel, F., 2003. Handbook of Inorganic Chemicals. McGraw-Hill, New York, NY.

Peng, Y., Cheng, E., 1993. Magnetic fusion driven transmutation of nuclear waste (FTW). Journal of Fusion Energy 12 (4), 381–384.

Rubbia, C., Aleixandre, J., Andriamonje, S., et al., 2001. A European Roadmap for Developing Accelerator Driven Systems (ADS) for Nuclear Waste Incineration. ENEA Report, 88–8286.

Speziale, C., Sarkar, S., Gatski, T., 1991. Modelling the pressure–strain correlation of turbulence: an invariant dynamical systems approach. Journal of Fluid Mechanics 227 (-1), 245–272.

Stacey, W., Abbasi, Z., Boyd, C., Bridges, A., Burgett, E., Cymbor, M., Fowler, S., Jones, A., Kelm, R., Kern, B., et al., 2006. A subcritical, helium-cooled fast reactor for the transmutation of spent nuclear fuel. Nuclear Technology 156 (1), 99–123.

Stacey, W., Beavers, V., Casino, W., Cheatham, J., Friis, Z., Green, R., Hamilton, W., Haufler, K., Hutchinson, J., Lackey, W., et al., 2005. A subcritical, gas-cooled fast transmutation reactor with a fusion neutron source. Nuclear Technology 150 (2).

Stern, F., Wilson, R., Coleman, H., Paterson, E., 2001. Comprehensive approach to verification and validation of CFD simulations – Part 1: Methodology and procedures. Transactions – American Society of Mechanical Engineers Journal of Fluids Engineering 123 (4), 793–802.

von Lensa, W., Nabbi, R., Rossbach, M., 2008. RED-IMPACT Impact of Partitioning, Transmutation and Waste Reduction Technologies on the Final Nuclear Waste Disposal. Forschungszentrum Jülich.

Wilson, R., Stern, F., Coleman, H., Paterson, E., 2001. Comprehensive approach to verification and validation of CFD simulations. 2: Application for RANS simulation of a cargo/container ship. Journal of Fluids Engineering 123 (4), 803–810.